



An experimental and numerical study of librational driven flow in planetary cores and subsurface oceans

J. Noir^{a,*}, F. Hemmerlin^a, J. Wicht^b, S.M. Baca^c, J.M. Aurnou^a

^a Department of Earth and Space Sciences, University of California, Los Angeles, CA 90095-1567, USA

^b Max Planck Institute for Solar System Research, 37191 Katlenburg-Lindau, Germany

^c Department of Neurobiology-David Geffen School of Medicine, University of California, Los Angeles, CA 90095-1763, USA

ARTICLE INFO

Article history:

Received 4 June 2008

Received in revised form 7 November 2008

Accepted 9 November 2008

Keywords:

Libration
Mercury
Earth's moon
Europa
Titan
Ganymede
Callisto
Io
Core
Subsurface ocean
Core-mantle coupling
Turbulence
Centrifugal instability

ABSTRACT

Many planetary bodies undergo forced longitudinal librations [Williams, J.G., Boggs, D.H., Yoder, C.F., Ratcliff, J.T., Dickey, J.O., 2001. Lunar rotational dissipation in solid body and molten core. *Journal of Geophysical Research-Planets* 106 (E11), 27933–27968; Comstock, R.L., Bills, B.G., 2003. A solar system survey of forced librations in longitude. *Journal of Geophysical Research-Planets* 108 (E9); Margot, J.L., Peale, S.J., Jurgens, R.F., Slade, M.A., Holin, I.V., 2007. Large longitude libration of mercury reveals a molten core. *Science* 316 (5825), 710–714]. Yet few studies to date have investigated how longitudinal libration, the oscillatory motion of a planet around its rotation axis, couples with its interior planetary fluid dynamics [e.g., Aldridge, K.D., Toomre, A., 1969. Axisymmetric inertial oscillations of a fluid in a rotating spherical container. *Journal of Fluid Mechanics* 37, 307; Tilgner, A., 1999. Driven inertial oscillations in spherical shells. *Physical Review E* 59 (2), 1789–1794]. In this study, we investigate, via laboratory experiments, the viscously driven flow in a spherical librating fluid cavity. We focus on libration frequencies less than or equal to the planetary rotation frequency (frequency ratios $f^* \leq 1$), moderate rotation rates (Ekman numbers $E = 10^{-4}$ to 10^{-5}) and a relatively broad range of librational amplitudes (libration amplitudes $10^\circ \lesssim \Delta\phi \lesssim 200^\circ$; Rossby numbers $0.03 \lesssim Ro \lesssim 5$). In addition we model flow in three different core geometries: full sphere, $r_{\text{inner}} \approx 0.6r_{\text{outer}}$ and $r_{\text{inner}} \approx 0.9r_{\text{outer}}$.

Direct flow visualizations in the laboratory experiment allow us to identify three distinct librational driven flow regimes. The transitions between these regimes are governed by critical values of the outer boundary layer Reynolds number, Re . For $Re \lesssim 20$ the flow is dominated by inertial modes. For $20 \lesssim Re \lesssim 120$ the system becomes unstable to longitudinal rolls that form beneath the outer boundary. This laminar instability initiates near the equator and is qualitatively similar to Taylor-Görtler instabilities. For $Re \gtrsim 120$ the flow in the vicinity of the outer boundary becomes turbulent.

For several librating planets with an internal fluid layer, estimates of Re and f^* lie in the range of values accessible in our laboratory experiment. Our results suggest that Mercury, Io, Europa and Titan may undergo boundary layer turbulence, whereas Earth's moon, Callisto and Ganymede may become unstable to laminar longitudinal rolls.

Published by Elsevier B.V.

1. Introduction

Longitudinal librations are time periodic variations in a planetary body's axial rate of rotation. Solar system bodies that undergo forced longitudinal librations include Mercury; the Earth's Moon; Mars' moons, Phobos and Deimos; the four Galilean satellites of Jupiter; and many of the moons of Saturn (Yoder, 1995; Comstock and Bills, 2003). Of these bodies, Mercury (Hauck et al., 2004;

Margot et al., 2007; Breuer et al., 2007; Williams et al., 2007), the Moon (Williams et al., 2001), Io, Europa and Ganymede (Anderson et al., 1996, 1998) are believed to have partially molten, central iron cores. Bodies that may have subsurface oceans include Europa, Callisto, Ganymede and Saturn's moons Enceladus and Titan (Anderson et al., 2001; Spohn and Schubert, 2003; Van Hoolst et al., 2008; Lorenz et al., 2008).

Orbital dynamics studies have shown that the following conditions are necessary for gravitational interactions to drive planetary libration (Murray and Dermott, 1999): (1) The planet must have an equatorially asymmetric mass distribution. (2) Its orbit must have a non-trivial eccentricity. (3) Its spin and orbital rates must

* Corresponding author. Tel.: +1 310 825 9296; fax: +1 310 825 2779.
E-mail address: jerome@ess.ucla.edu (J. Noir).

be commensurate. The equation for the axial torque on a body with moments of inertia $A < B < C$ that is orbiting about a more massive body of mass M is

$$T = -\frac{3}{2} \frac{GM(B-A)}{r^3} \sin 2\gamma, \quad (1)$$

where r is the distance between the two bodies and γ describes the angle between the long equatorial axis of the smaller body and the line connecting it to the body it orbits. If the planet's mass distribution is symmetric about the equator, then $B - A = 0$ and there will be no axial torque on the body. If orbital and rotational rates of the body are not commensurate, then γ will vary so that the torque averaged over an orbital cycle is effectively zero (Comstock and Bills, 2003). For the case of an eccentric, synchronous orbit, the body's long equatorial A -axis will undergo quasi-periodic misalignments from the line perpendicular to gravitational equipotential surfaces. In a body with its rotation axis parallel to its orbit normal, the resulting axial torques tend to drive an oscillation superposed on the body's mean rotational rate (Balogh and Giampieri, 2002). Thus, at leading order, a body in synchronous orbit will typically librate once per orbital cycle. At the next order, the libration is an order of magnitude smaller in amplitude and oscillates twice per orbital cycle. Such higher order librational modes will not be considered here.

Angular momentum exchange between a planet's solid shell and a surrounding atmospheric envelope can also generate a planetary libration. For instance, on Earth, seasonal variations in atmospheric angular momentum produce observable changes in the planet's length of day (LOD) (Wahr, 1988). The seasonal LOD variations correspond to a small $\lesssim 0.3$ arcsecond librational motion, with a nearly yearly oscillation period. In contrast, a much larger seasonal libration may occur on Titan, which has a relatively massive atmosphere and strong seasonal zonal wind variations. Recent Cassini and Hubble Space Telescope measurements reveal that Titan's rotation rate is varying over a roughly year time-scale (e.g., Lorenz et al., 2008). These measurements indicate that Titan's May 2007 rotation rate is $+0.36^\circ/\text{year}$ greater than its rotation rate measured in October 2004. This super-rotation is likely due to libration of Titan's outermost solid shell, driven by seasonal variations in its atmospheric zonal wind field (Tokano and Neubauer, 2005). Given a seasonal libration period of 14.75 years and assuming a simple, constant prograde rotation rate of $+0.36^\circ/\text{year}$ for half a libration period, we arrive at an estimated libration amplitude of $\Delta\phi \simeq 2.5^\circ$ for Titan. Although this crude amplitude estimate likely represents an upper bound (Van Hoolst et al., 2008), it shows that seasonally driven librations can be substantial on this body.

Measuring a planet's libration can provide constraints in models of its interior structure (Peale and Boss, 1977; Wu et al., 1997; Peale et al., 2002; Margot et al., 2007; Van Hoolst et al., 2008). For example, Margot et al. (2007) have shown that Mercury's libration amplitude can be explained by a mantle decoupled from the deep interior by a liquid shell. Van Hoolst et al. (2008) have proposed a dynamical libration model of Europa, for which the measurement of its librational parameters can provide constraints on the existence of a subsurface ocean and on the thickness of the surrounding ice shell. However in such models, it is typically argued that the liquid shell is only coupled to the overlying solid spherical shell through a laminar viscous boundary layer (e.g., Peale and Boss, 1977; Van Hoolst et al., 2008) and that the interior of the fluid layer remains in solid body rotation. Such a coupling does not produce significant internal dissipation and is therefore neglected in the energy budget of the planets.

In contrast, it has been proposed by Kerswell and Malkus (1998) that librational flows inside Io's liquid outer core may be responsible for its magnetic signature. Kerswell and Malkus argue

that the estimated equatorial ellipticity of Io's CMB is sufficient to produce elliptical instability, a pairwise resonance of inertial waves (Kerswell and Malkus, 1998). In the presence of Jupiter magnetic field the flow associated with the elliptical instability inside the molten core will generate an induced magnetic field. However, the typical magnetic field signature as well as the detailed structure of the librational driven elliptical instability have yet to be determined.

In general, the solid boundary surrounding an internal liquid layer of a planet is a triaxial ellipsoid. Both pressure and viscous coupling between the librating solid boundary and the liquid layer can generate secondary fluid motions. A fundamental difference between the pressure and the viscous forcing is their azimuthal symmetry, respectively, $m = 2$ and $m = 0$ (axisymmetric). Thus, the pressure and viscous torque are expected to produce very different dynamics. In order to separate the flow in the liquid layer driven by each forcing we must consider the following two cases. In the first case, which is the purpose of the present study, the shell is spherical and the only coupling between the longitudinally librating outer solid shell and the liquid layer is viscous. In the second case, the equatorial ellipticity is large enough so that the pressure coupling between the surrounding longitudinally librating solid shell and the liquid dominates. The second case is beyond the scope of the present paper and will be investigated in a future experimental study.

The flow induced inside a rapidly rotating, spherical fluid cavity by the libration of its container has been investigated by Aldridge (1967), Aldridge and Toomre (1969), Aldridge (1975) and Tilgner (1999). Tilgner (1999) investigated the linear response of a fluid spherical shell with various inner core radii via a suite of numerical simulations. He showed that the linear response to librational forcing is comprised of inertial modes, which are the eigenmodes of a rapidly rotating fluid cavity (Greenspan, 1968). For moderate inner core sizes, Tilgner demonstrated that the presence of an inner core only marginally modifies the resonance frequencies and other global observables, such as kinetic energy density. Aldridge and Toomre (1969) carried out laboratory experiments to investigate the librational driven flow in a spherical fluid cavity. Using pressure differences between two points on the axis of rotation, they identified resonances of axisymmetric inertial modes at oscillation frequencies predicted theoretically by Greenspan (1968). In addition, Aldridge (1967) reported that axisymmetric vortices with vorticity in the azimuthal $\hat{\phi}$ -direction – so-called 'longitudinal rolls' – develop near the outer boundary of the cavity at higher libration amplitudes.

We investigate the simplest model of flow inside a liquid layer (outer core or subsurface ocean) driven by the forced longitudinal libration of a solid outer spherical shell (mantle or ice shell). In particular, we focus on the viscous coupling between the underlying liquid and the surrounding shell in a range of boundary layer Reynolds numbers that are relevant to planets (see Table 2).

We present the results of a systematic study of librational core-flow in spherical geometry that seek to expand upon these earlier studies. In particular, we determine the transition between the regime dominated by inertial modes in the bulk of the fluid (e.g., Tilgner, 1999), the longitudinal roll regime first noted by Aldridge (1967) and a librational driven turbulence regime that has not been previously reported.

The paper is organized as follows. In Section 2 we present the governing equations and the control parameters. Section 3 presents the laboratory setup and the numerical model that we use to illustrate the fundamental flows that arise in our laboratory experiment. The results are presented in Section 4. In Section 5 we discuss how to extrapolate our findings to planetary core conditions. Finally, a synopsis of our findings is given in Section 6.

2. Governing equations and control parameters

In the present study we consider a spherical fluid cavity of outer radius r_o and an inner core of radius r_i . We assume the fluid to be electrically non-conductive. The equations governing the motion of an incompressible, homogeneous fluid in a rotating spherical shell are

$$\frac{\partial \mathbf{u}}{\partial t} + \mathbf{u} \cdot \nabla \mathbf{u} + 2\Omega \hat{\mathbf{z}} \times \mathbf{u} = -\frac{1}{\rho} \nabla p + \nu \nabla^2 \mathbf{u}, \quad (2)$$

$$\nabla \cdot \mathbf{u} = 0, \quad (3)$$

where $\bar{\mathbf{u}}$ is the velocity measured in the rotating reference frame; $\Omega \hat{\mathbf{z}}$ is the mean angular velocity vector; ρ denotes the constant fluid density; p is the modified pressure that contains the gravitational and centrifugal potentials; and ν is the fluid's kinematic viscosity.

The librational forcing enters the problem through the velocity boundary condition on the outer boundary r_o ,

$$u_\phi(r_o) = (r_o \cos \theta)[(\Delta\phi\omega_L) \sin(\omega_L t)]. \quad (4)$$

Here θ denotes latitude, $\Delta\phi$ is the angular amplitude of libration in radians and ω_L is the angular velocity of libration in rad/s. We define the retrograde phase of the libration cycle as the period during which $u_\phi(r_o) < 0$ and the prograde phase as the period during which $u_\phi(r_o) > 0$. This sinusoidal motion of the container mechanically forces flow in the underlying fluid through viscous boundary stresses.

2.1. Dimensionless equations and control parameters

Eqs. (2)–(4) are non-dimensionalized using Ω^{-1} and the outer radius r_o , as the respective units of time and length. The non-dimensional form of the equations then becomes

$$\frac{\partial \mathbf{u}}{\partial t} + \mathbf{u} \cdot \nabla \mathbf{u} + 2\hat{\mathbf{z}} \times \mathbf{u} = -\nabla p + E \nabla^2 \mathbf{u}; \quad (5)$$

$$\nabla \cdot \mathbf{u} = 0; \quad (6)$$

subject to

$$u_\phi(r_o) = Ro \sin \theta \sin(f^* t). \quad (7)$$

The Ekman number, E , is a measure of the ratio of the viscous and the Coriolis forces:

$$E = \frac{\nu}{\Omega r_o^2}. \quad (8)$$

The Rossby number, Ro , measures the relative strength of the librational forcing to the Coriolis force:

$$Ro = \Delta\phi f^*, \quad (9)$$

where the frequency ratio

$$f^* = \frac{\omega_L}{\Omega} \quad (10)$$

is the ratio of the libration and the background rotation frequencies. Lastly, the radius ratio

$$\chi = \frac{r_i}{r_o} \quad (11)$$

describes the spherical shell geometry.

2.2. Boundary layer Reynolds number

The flow inside the fluid cavity is effectively inviscid; at first order the differential motion between the librating shell and the rotating fluid is accommodated in a thin viscous boundary layer beneath the outer wall, which is called the Ekman boundary layer. Anticipating the relevance of non-linear terms in this outermost

Table 1

Physical and dimensionless parameter definitions and their typical values in the laboratory experiment.

Parameter	Definition	Experiment
r_o	Outer boundary radius	8.5 cm
r_i	Inner boundary radius	0, 5.1 cm, 7.65 cm
$\Omega/2\pi$	Mean rotation rate	5–60 rpm
$\omega_L/2\pi$	Libration frequency	0.1–2 Hz
$\Delta\phi$	Angular displacement	0–180°
ν	Kinematic viscosity	10 ⁻⁶
χ	r_i/r_o	0, 0.6, 0.9
E	$\nu/\Omega r_o^2$	10 ⁻⁵ – 10 ⁻³
f^*	ω_L/Ω	0.4–1
Ro	$\Delta\phi f^*$	0.03–5
Re	$Ro E^{-1/2}$	0–400

region of the fluid, we introduce the outer boundary layer Reynolds number, Re . This parameter measures the relative strength of inertial and viscous forces in the Ekman boundary layer. It is defined as

$$Re = \frac{u\delta}{\nu},$$

where we use the Ekman boundary layer thickness $\delta = (\nu/\Omega)^{1/2} = E^{1/2} r_o$ (Greenspan, 1968) as the characteristic length scale and the peak equatorial velocity of the shell $u = \Delta\phi\omega_L r_o$ as the characteristic velocity scale. This yields

$$Re = \frac{\Delta\phi\omega_L r_o}{(\nu\Omega)^{1/2}} = \Delta\phi f^* E^{-1/2} = Ro E^{-1/2}. \quad (12)$$

Note that Re is independent of the size of the inner core in expression (12). Thus, we expect an inner core to have no significant effect in systems where Re controls the instabilities in the outer boundary layer.

Typical laboratory values of the parameters introduced above are given in Table 1, planetary counter part are given in Table 2. For example, we estimate $E \sim 10^{-13}$; $Ro \sim 10^{-4}$; $f^* = 2/3$; and $Re \sim 500$ for Mercury. In comparison, our laboratory and numerical experiments are carried out at $10^{-5} \lesssim E \lesssim 10^{-4}$; $0.03 \lesssim Ro \lesssim 5$; $0 < f^* < 1$; and $10 \lesssim Re \lesssim 400$. Thus, our experiments can match the f^* and Re values typical of librating planets (Tables 1 and 2). However, due to the moderate Ekman number values accessible in our present experiments, these Reynolds numbers can be reached only by using libration amplitudes ($0.2 \lesssim \Delta\phi \lesssim 3.5$ rad) that greatly exceed planetary values ($10^{-6} \lesssim \Delta\phi \lesssim 10^{-4}$ rad).

3. Methods

3.1. Laboratory experimental set-up

Fig. 1 shows a schematic view of the apparatus used in the present study. The acrylic container consists of a right cylinder (9.9 cm outer radius) with an internal spherical cavity (8.5 cm radius). The cavity is filled with room temperature water. The librational motion of the outer shell is simulated using two motors. The torsional oscillation of the acrylic container is directly driven by a 400 W ring-style servomotor (Yaskawa SGMCS-10C3B11). We use a motion control card (Trio MC202) to set the sinusoidal oscillation of the servomotor. The container and the ring-servo are centered on the upper deck of a 1 m diameter turntable, which simulates the mean rotation rate of the planet. The rotation rate of the turntable is belt-driven by a one horse-power DC motor (Marathon Blackmax Y535) with a 6:1 gear-head reducer and an inverter drive (Yaskawa CIMR-F7U20P71). The servo motor is capable of oscillating the container at frequencies, $f_L = \omega_L/2\pi$, between 0.1 and 2.0 Hz with an angular amplitude, $\Delta\phi$, that ranges from 2.5° to 360°

Table 2
Physical and dimensionless parameters values for planets, listed from top to bottom in terms of increasing boundary layer Reynolds number value. Titan(Grav) and Titan(Atm) correspond to Titan's forced longitudinal librations driven, respectively, by gravitational coupling and by atmospheric circulation. The anagram SO and LC stand for subsurface ocean and liquid metal core. Unless specified, the amplitudes of libration are from Comstock and Bills (2003). We use viscosities $\nu = 10^{-6}$ and $\nu = 3^{-7} \text{ m}^2/\text{s}$, respectively, for subsurface oceans and molten iron rich core. T_{spin} is the rotational period of the planet.

Planets	Internal layer	r_o (km)	r_i (km)	T_{spin} (day)	f^*	$\Delta\phi$ (rad)	E	Ro	Re
Callisto ^{a,b}	SO	~2300	2000–2300	16.68	1	4.22×10^{-6}	4×10^{-14}	4.22×10^{-6}	~20
Ganymede ^{c,d}	LC	~800	0–500	7.15	1	5.64×10^{-6}	4×10^{-14}	5.64×10^{-6}	~25
Earth's moon ^e	LC	~350	0–150	27.3	1	7×10^{-5}	10^{-12}	7×10^{-5}	~73
Titan(Grav) ^{f,g}	SO	~2500	2350–2450	15.95	1	2.3×10^{-5}	3.5×10^{-14}	2.3×10^{-5}	~123
Mercury ^h	LC	~1800	0–1700	58.6	2/3	2×10^{-4} h	7.5×10^{-14}	1.33×10^{-4}	~490
Titan(Atm) ^{f,g}	SO	~2500	2350–2450	15.95	3×10^{-3}	4.36×10^{-2} f	3.5×10^{-14}	1.3×10^{-4}	~690
Io ⁱ	LC	~500	–	1.77	1	1.3×10^{-4}	3×10^{-14}	1.3×10^{-4}	~800
Europa ^j	SO	~1450	1300–1400	3.55	1	2×10^{-4} j	$.23 \times 10^{-14}$	2×10^{-4}	~1300

^a Kuskov and Kronrod (2005).

^b Spohn and Schubert (2003).

^c Hauck et al. (2006).

^d Sohl et al. (2002).

^e Williams and Dickey (2002).

^f Lorenz et al. (2008).

^g Tobie et al. (2005).

^h Margot et al. (2007).

ⁱ Anderson et al. (2001).

^j Van Hoolst et al. (2008).

(0.04 to 3.14 rad, respectively). We monitor the oscillation using the ring-servo's optical encoder. The oscillatory motion follows a true sinusoid to within $\pm 0.25\%$ for typical runs ($\Delta\phi = 15 - 45^\circ$; $f_L = 0.05$ to 1.0 Hz) and to within $\pm 1.5\%$ for the most extreme cases ($\Delta\phi = 140^\circ$; $f_L = 2.0$ Hz). The rotation rate of the turntable can be set from 1 to 60 rpm (0.017 to 1 Hz, respectively) and is stable to better than $\pm 0.5\%$. Some of the experiments use a solid acrylic inner core. The two inner core sizes used are $r_i = 5.1$ and 7.65 cm. In all experiments, only the outer shell librates; the inner core rotates at the constant background angular velocity Ω . The parameter values accessible with this device are given in Table 1.

In our experiments the working fluid is seeded with Kalliroscope flakes to visualize shear zones in the fluid (e.g., Noir et al., 2001a). Boundary layer flow characterizations are carried out with high concentrations of Kalliroscope flakes, which make the volume of fluid opaque except for the first mm or so near the outer wall. For outer boundary flow visualizations, photographic flash and high intensity LED's (Luxeon III's) are used as light sources for still images and movies, respectively. Shear zones in the fluid inter-

rior are visualized using a 1/1000 solution of Kalliroscope and a light sheet produced by a 24 mW diode-laser (Roithner LaserTechnik). Flow visualizations are made with cameras and lights sources in the rotating frame. Still images are acquired using a standard digital SLR (Canon EOS Rebel). Movies are made using a high sensitivity CCD camera (Watec WAT-902H2). The analog movie signal is sent via a wireless system from the rotating frame to an analog-to-digital video converter (Canopus ADVC-110) in the laboratory frame. The output from the converter is then fed into a data acquisition computer, which records the movies at 30 frames per second (BTV Pro software). This imaging system is a modified version of that described in Baca et al. (2005).

Each libration experiment follows a similar protocol. First the turntable rotates for ~ 5 to 15 min to enable the fluid to spin-up to solid body rotation. Then, the ring-servo is activated to oscillate the acrylic container. The resulting flow inside the cavity typically equilibrates within ~ 10 oscillation periods. Flow imaging is then carried out.

3.2. Numerical modeling

In addition to the laboratory experiments, we have carried out two numerical simulations of flow driven by outer-boundary librational motion. We use a modified version of the code MagIC3.16 (Wicht, 2002) to numerically solve Eqs. (2)–(4). This fully nonlinear, three-dimensional code makes use of the pseudo-spectral methodology first introduced by Glatzmaier (1984). It has been previously used to simulate thermal convection and dynamo action in rapidly rotating spherical shells of Boussinesq fluid (e.g., Wicht, 2002; Heimpel et al., 2005; Aurnou et al., 2007). A detailed description of this model is given in Christensen and Wicht (2007).

The two simulations are carried out at an Ekman number of $E = 10^{-4}$, a libration frequency of $f^* = 2/3$, a spherical shell radius ratio of $\chi = 0.35$, and Rossby numbers of $Ro = 0.1$ and 1, corresponding to $Re = 10$ and $Re = 100$, respectively. Both simulations use a grid having 61 radial levels, 64 points in colatitude and 128 points in full azimuth. The associated spectral space contains spherical harmonics up to degree and order of 42 and 40, respectively, and 59 Chebyshev polynomials in radius. In order to increase our computational efficiency, we use an 8-fold azimuthal symmetry to solve the equations (e.g., Al-Shamali et al., 2004). The mechanical boundary conditions are no-slip on r_i and r_o . Each simulation is

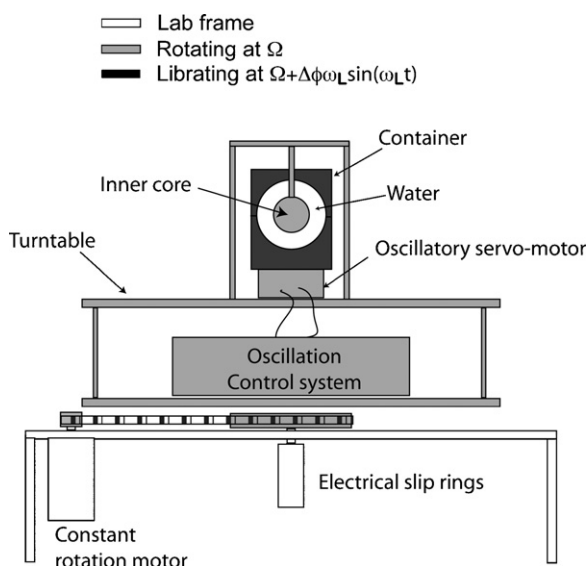


Fig. 1. Schematic view of the laboratory experiment.

initialized with a small, random velocity field perturbation from which instabilities may develop. The outer shell librates while the inner core rotates at the background rotation rate. Thus, viewed in the rotating frame, the inner core is fixed while the outer shell oscillates.

4. Results

Our laboratory models of librationaly driven flow have been carried out over approximately one decade of Ekman numbers, $2 \times 10^{-5} < E < 10^{-4}$. In this section, we report laboratory observations for $E = 2 \times 10^{-5}$ and increasing values of the Rossby number. However, the same succession of regimes is observed at all values of the Ekman number investigated.

In the laboratory experiments we observe three different libration-driven flow regimes. For weak librational forcing, no instabilities are observed in the interior or near the container boundary (stable regime). For moderate forcing, we observe longitudinal rolls forming just beneath the outer boundary (longitudinal roll regime). For large librational forcing, turbulence develops in the outermost region of the fluid (boundary turbulence regime). The two numerical simulations we carry out at $Re = 10$ and $Re = 100$ are, respectively, in the stable and longitudinal roll regimes.

4.1. The stable regime

The numerical simulations carried out at low librational forcing ($E = 10^{-4}$, $Ro = 0.1$, $Re = 10$) reveals oblique oscillatory shear layers in the fluid interior characteristic of inertial waves (Fig. 2a–c), in agreement with Tilgner (1999). The oscillating shear layers arise due to a local breakdown of the Ekman boundary layer at the so-called critical latitude, which results in a discontinuity of the velocity field. The discontinuity propagates inside the volume along conical shear layers aligned with the axis of rotation. In a meridional plane the intersected conical structures form a ray pattern as seen in Fig. 2a–c (e.g., Tilgner, 1999; Noir et al., 2001b). The critical latitude Θ_c and the angle between the axis of rotation and the shear layer Ψ depend on the dimensionless oscillation frequency f^* as:

$$\cos \Theta_c = \sin \Psi = \frac{f^*}{2}.$$

The thickness of the internal shear layer scales as $E^{1/5}$ and the associated tangential velocities scale as $RoE^{2/5}$ (Stewartson and Roberts, 1963; Noir et al., 2001b), both of which are small at planetary conditions. Thus, we do not expect these oblique shear layers to contribute significantly to global observables such as the kinetic energy and the viscous dissipation.

In addition, Fig. 2b shows that libration of the outer shell induces a significant meridional circulation u_θ in the Ekman boundary layer. During the prograde phase of the libration cycle, the Ekman circulation in the boundary layer is directed from the poles to the equator. During the retrograde phase of the cycle, this circulation is directed polewards.

For laboratory experiments at $E = 2 \times 10^{-5}$ and $Ro \lesssim 0.1$ ($Re \lesssim 20$), direct flow visualizations do not reveal oblique shear structures in the interior of the fluid. However, the rapidly oscillating inertial waves are known to be difficult to observe in laboratory experiments which use Kalliroscope visualization (Noir et al., 2001a). Thus, it is likely that an inertial wave field exists in our laboratory experiments that is similar to the numerical simulation. Quantitative velocity measurements such as laser or acoustic Doppler velocimetry will allow for their detection in future laboratory experiments.

4.2. Longitudinal rolls

In laboratory experiments with $E = 2 \times 10^{-5}$, $0.1 \lesssim Ro \lesssim 0.8$ ($20 \lesssim Re \lesssim 120$), and $\chi = [0, 0.6, 0.9]$, the flow beneath the outer boundary, at $r = r_o$, is unstable periodically in time. The time evolution of the system is illustrated in Fig. 3.

The flow beneath the outer boundary becomes unstable predominantly during the retrograde phase of the cycle, and then relaminarizes during the prograde phase of each libration cycle. Thus, this represents a transiently unstable system (e.g., Davis, 1976). This process is described in detail in the following paragraphs.

Near the end of the prograde phase of each libration cycle, two quasi-axisymmetric shear zones develop on either side of the equator. During the retrograde phase of the libration cycle, these shear structures travel symmetrically to higher latitudes (Fig. 4). Movies of the interior flow suggest that each quasi-axisymmetric shear zone is associated with a single roll with its vorticity oriented in the ϕ -direction. We refer to these quasi-axisymmetric structures as “longitudinal rolls”. The region between the equator and the initial poleward propagating longitudinal rolls is referred to here as “the curtain” (Fig. 4b). We hypothesize that the poleward spreading of the curtain results from the advection of the longitudinal shear structures by the Ekman circulation.

Shortly after the curtain starts expanding poleward, we typically observe distinct longitudinal rolls that form within the curtain region (Fig. 5a). For large enough angular displacements, these secondary roll structures are also advected poleward. As the container enters the prograde phase of motion, the longitudinal rolls dissipate, sometimes becoming wavy as they do so. The instability pattern shown in Fig. 5a occurs during the retrograde phase of the libration cycle. Secondary longitudinal rolls do not develop during the prograde phase of the cycle.

The same transient instability process repeats during each libration cycle; the position at which the rolls form is consistent from one cycle to another. The instability patterns are qualitatively similar to Taylor instabilities in differentially rotating cylinders (Coles, 1965; Andereck et al., 1986) and spherical shells (Nakabayashi et al., 2002), to Taylor-Görtler instabilities observed in cylindrical spin-down experiments (Weidman, 1976a, b; Neitzel and Davis, 1981) and in oscillating cylinder simulations (Blennerhassett and Bassom, 2007).

The longitudinal rolls are observed to develop only in the outermost region of the fluid. No such structures are detected in the fluid interior. Instead, we observe steady vertical (geostrophic) shear zones in the bulk of the fluid through the entire libration cycle. Similar observations of steady geostrophic shear zones have been reported by Malkus (1968), Vanyo et al. (1995) and Noir et al. (2001a, b). They are interpreted as the results of non-linear interaction in the Ekman boundary layer.

In order to investigate the effect of a solid inner core on the longitudinal roll instability, we have carried out experiments with three different non-librating inner cores ($\chi = 0, 0.6$ and 0.90). In the range of parameters accessible with our device, we do not observe any measurable effect of an inner core on the instabilities.

We have carried out a numerical simulation at $Re = 100$ with $E = 10^{-4}$, $Ro = 1$, $f^* = 1$ and $\chi = 0.35$ for comparison with our laboratory results in the longitudinal rolls regime. Fig. 2d–f show meridional slices of the azimuthally averaged velocity components near the end of the retrograde phase of motion. Fig. 5b shows the shear structures below the outer boundary at the end of the retrograde phase of motion. The signature of the longitudinal rolls is clearly identified in the radial component of the velocity field shown in Figs. 2d and 5b. Numerical movies of the velocity field reveal a poleward motion of the longitudinal rolls during the ret-

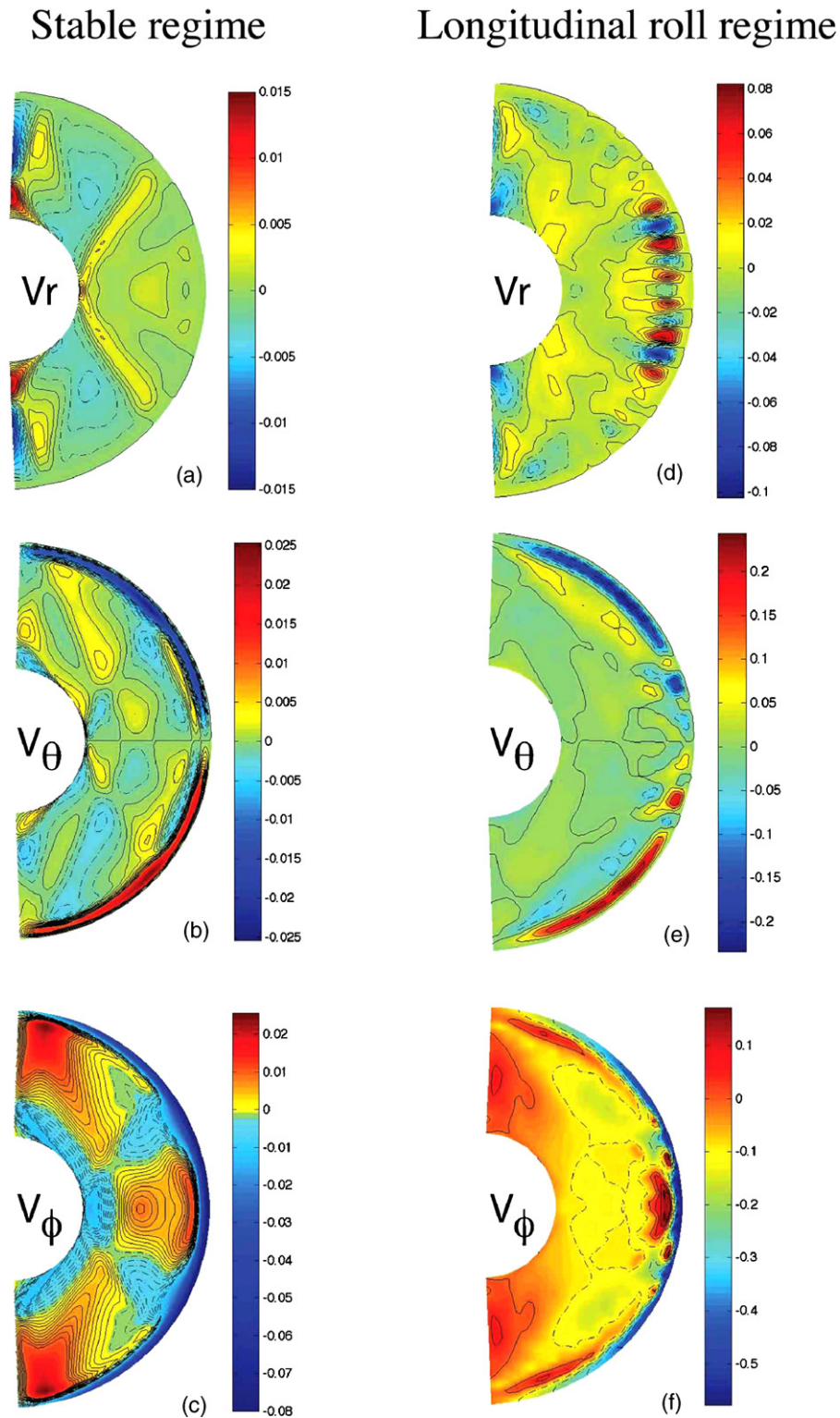


Fig. 2. Axisymmetric velocity fields in a meridional plane from numerical simulations with $E = 10^{-4}$, $f^* = 1$, $\chi = 0.35$: (a, d) radial velocities; (b, e) colatitudinal velocities; (c, f) azimuthal velocities. All panels are snapshot of the velocity at a time corresponding to the maximum retrograde rotation rate of the shell. Left panels (a, b, c) $Ro = 0.1$, $Re = 10$; right panels (d, e, f) $Ro = 1$, $Re = 100$. The velocity scale bars are all in the non-dimensional units of $u/\Omega r_0$.

rograde phase of the libration cycle for this simulation. In contrast to the $Ro = 0.1$ simulation (Fig. 2a–c), inertial waves do not dominate the interior flow field in the $Ro = 1$ simulation. Furthermore, a comparison of panels 2b and e shows that the Ekman circulation is significantly modified in the region where longitudinal rolls develop.

Note that the $Ro = 1$ simulation produces axisymmetric roll structures, even though the code allows three-dimensional flows (Fig. 5b). This differs from the laboratory experiments, which often generate wavy roll structures near the end of the retrograde libration (Fig. 5a). The axisymmetric numerical results are likely caused by the 8-fold azimuthal symmetry that we have imposed on the

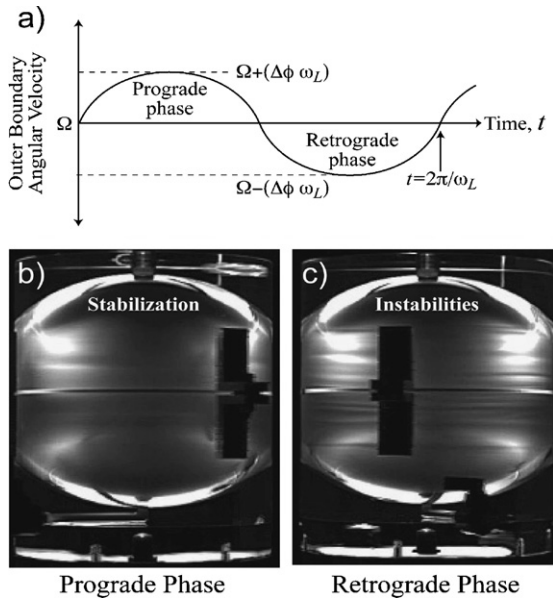


Fig. 3. (a) Schematic showing the angular velocity of the librating container. Experimental sideview images (b) of stable boundary layer flow during the prograde phase of the libration cycle and (c) of the longitudinal rolls that develop during the retrograde phase of the cycle.

solutions. Thus, the development of non-axisymmetric flow is inhibited in our numerical simulations.

4.3. Turbulence

In laboratory experiments with $E = 2 \times 10^{-5}$ and $Ro \gtrsim 0.8$ ($Re \gtrsim 120$), we observe complex non-axisymmetric structures below the container’s outer wall (Fig. 6). Kalliroscope movies show that these structures vary significantly both in time and space. We consider such flows to be turbulent. However, in the absence of quantitative velocity data, determining the onset of boundary turbulence is somewhat subjective.

For weakly turbulent cases, a set of longitudinal rolls form during the retrograde phase of libration. These rolls first become wavy and then become unstable to smaller scale structures near the end of the retrograde phase of the cycle. In addition, we observe the vestige of the longitudinal roll pattern throughout the retrograde phase of the libration cycle. In these weakly turbulent cases, the

flow relaminarizes completely during the prograde phase of each libration cycle.

In more strongly forced cases, we observe that the longitudinal rolls become unstable earlier into the retrograde phase of the cycle (Fig. 6). In experiments carried out using large angular displacements ($\Delta\phi \gtrsim 50^\circ$), a poleward advection of the turbulent structures is also observed. At the peak of their development, the turbulent structures no longer exhibit symmetry correlated with the longitudinal roll pattern. The turbulent instability always peaks during the retrograde phase of the libration cycle and decays during the prograde phase. However, the turbulence does not completely dissipate during the prograde phase and, thus, may persist throughout the entire libration cycle.

Fig. 6b shows shear structures in a meridional slice for a full sphere geometry ($\chi = 0$) in the turbulent regime. The turbulent flow structures occupy the outermost portion of the fluid. In the interior of the fluid, the flow remains predominantly laminar and is characterized by vertical (geostrophic) shear zones, as in the longitudinal rolls regimes. In further similarity to the longitudinal rolls regime, the size of the inner core does not measurably affect the boundary turbulence.

4.4. Regime diagram

Fig. 7 is a compilation of all the experimental observations made in this study represented in a (E, Re) parameter space. We vary the Ekman number by changing the rotation rate of the turntable and we vary the Rossby number by adjusting the oscillation frequency and the angular displacement of the ring-servo motor. Experiments in the stable boundary layer regime are represented in blue symbols; the longitudinal roll instability cases are represented by green symbols; and the turbulent regime cases are represented by red symbols. The different symbols shapes correspond to the three inner core sizes used in the laboratory experiment. The $\chi = 0$ full sphere geometry cases are marked by circles (\circ); the $\chi = 0.6$ cases are marked by inverted triangles (∇); the $\chi = 0.9$ cases are marked by squares (\square).

The results shown in Fig. 7 suggest that the onset of the longitudinal roll and of the boundary turbulence regimes are consistent with critical boundary layer Reynolds numbers, respectively, of $Re_{c1} \simeq 20$ and $Re_{c2} \simeq 120$ (Fig. 7). The critical Re values are comparable with those characteristic of Ekman boundary layer instabilities with steady or oscillating forcings (Faller, 1963; Faller and Kaylor, 1966; Lilly, 1966; Tatro and Mollo-Christensen, 1967; Aelbrecht et al., 1999). Due to the limited range of accessible Ekman numbers

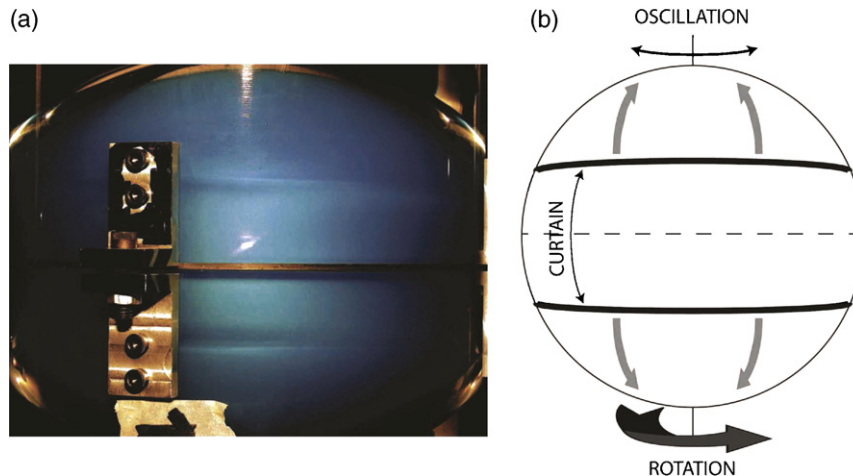


Fig. 4. (a) Laboratory flow visualization using Kalliroscope showing curtain development in the outer boundary layer ($E = 5 \times 10^{-5}$ [$\Omega = 20$ rpm], $f^* = 2/3$, $Ro = 0.7$ [$\Delta\phi = \pi/3$] and $\chi = 0$). (b) Schematic of curtain development.

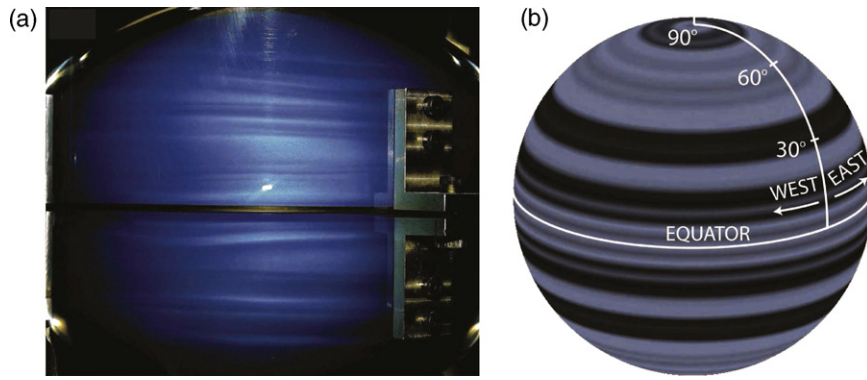


Fig. 5. Longitudinal rolls beneath the outer boundary. (a) Laboratory experiment at $Re = 100$ ($E = 5 \times 10^{-5}$ [$\Omega = 20$ rpm], $f^* = 2/3$, $Ro = 0.7$ [$\Delta\phi = 60^\circ$], and $\chi = 0$). (b) The θ -derivative of the radial velocity component, $\partial u_r / \partial \theta$ from the numerical simulation at $Re = 100$ with $E = 10^{-4}$, $Ro = 1$, $f^* = 1$ and $\chi = 0.35$.

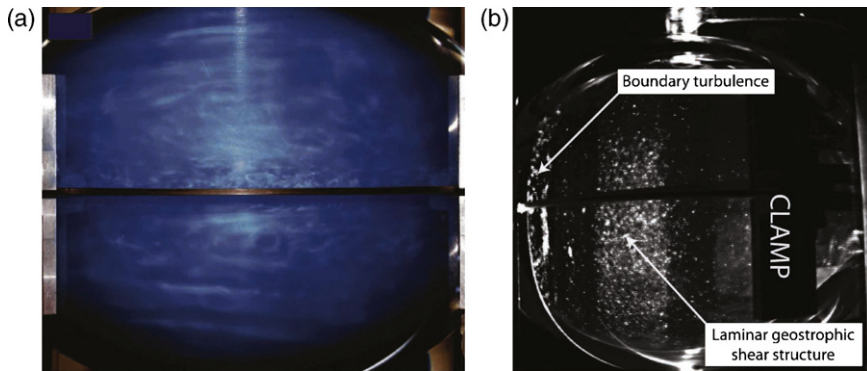


Fig. 6. Laboratory flow visualization using Kalliroscope in the boundary turbulence regime at $Re = 134$ ($E = 10^{-4}$, $Ro = 1.34$, $\chi = 0$ and $f^* = 1$). (a) Boundary flow beneath the outer wall; (b) interior flow along a meridional section of the fluid cavity.

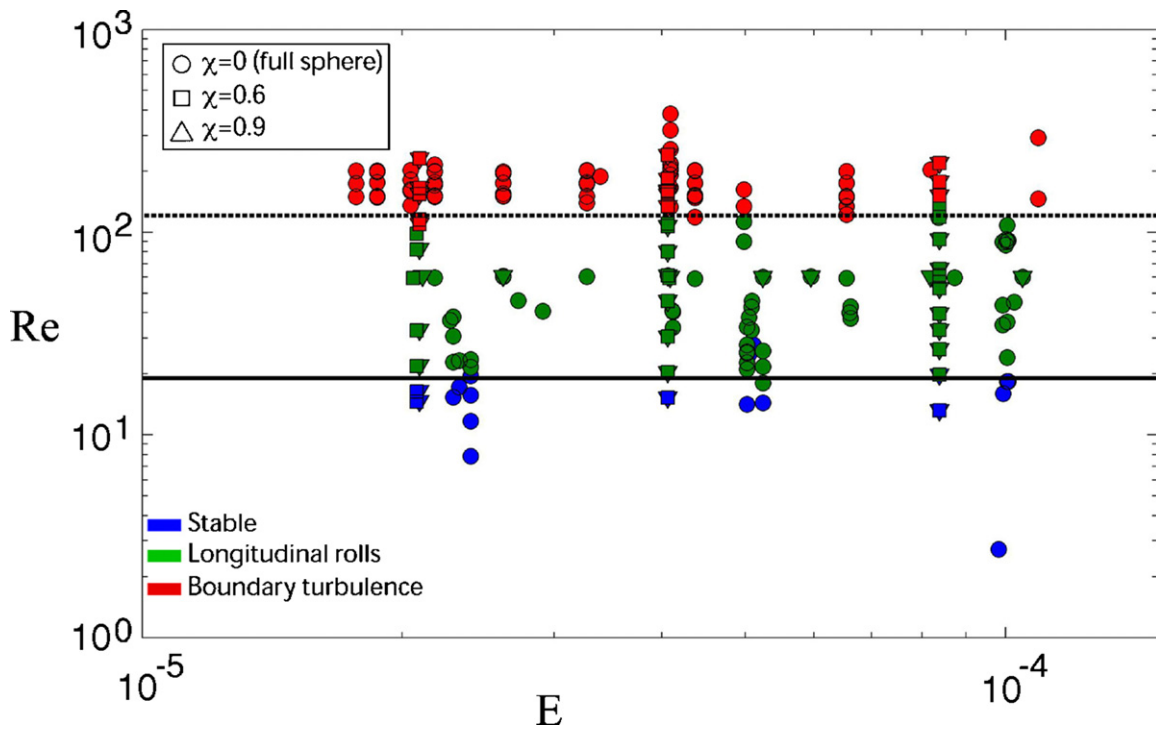


Fig. 7. Compiled experimental results plotted in terms of Re versus E . Flow regimes: stable boundary layer (blue); longitudinal roll instability (green); outer boundary turbulence (red). The symbol's denotes inner core size: full sphere $\chi = 0$ (\circ); $\chi = 0.6$ (\square); $\chi = 0.9$ (∇). The critical boundary layer Reynolds number are represented by black solid ($Re_{c1} = 20$) and dashed ($Re_{c2} = 120$) lines, respectively, for the onset of the longitudinal rolls and boundary turbulence. (For interpretation of the references to color in this figure legend, the reader is referred to the web version of the article.)

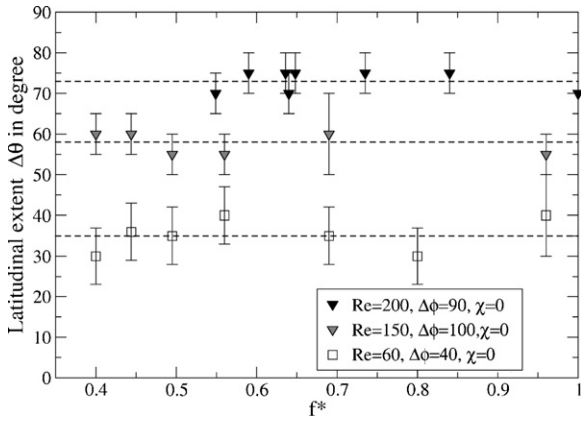


Fig. 8. Latitudinal extent $\Delta\theta$ as a function of f^* for fixed ($Re = 60, \Delta\phi = 40^\circ$) in the longitudinal roll regime; ($Re = 150, \Delta\phi = 100^\circ$) and ($Re = 200, \Delta\phi = 90^\circ$) in the boundary turbulence regime. The dashed lines represent the mean value of each data set, respectively, $35^\circ, 58^\circ$ and 73° for $Re = 60, 150$ and 200 .

and to the subjectivity inherent to direct visualization we have not considered higher order scaling laws, e.g. $Re_c = Ro^\alpha E^\beta$. Thus, the validity domain of these scaling laws will have to be ascertained in future work at lower E values.

4.5. Latitudinal extent of instabilities

The results shown in Fig. 7 imply that Re controls the regime transitions in our laboratory experiments. We now seek to determine how the latitudinal extent of the unstable region evolves as we lower Ro and E (towards planetary values) for fixed Reynolds numbers. We define the latitudinal extent $\Delta\theta$ as the maximum latitude at which we observe structures characteristic of a particular regime.

As we decrease E from 10^{-4} to 2×10^{-5} , the Rossby number must satisfy $Ro = ReE^{1/2}$ in order to maintain a fixed value of Re . Using the definition $Ro = \Delta\phi f^*$, this can be achieved in two different ways. First, at a fixed amplitude of libration $\Delta\phi$, this is accomplished by lowering the frequency f^* . Second, at fixed frequency f^* , this is accomplished by decreasing the amplitude of libration $\Delta\phi$.

In Fig. 8 we consider three different pairs of fixed ($Re, \Delta\phi$) and vary f^* and E in order to determine the dependency of the latitudinal extent of the instability on f^* as E is lowered toward planetary conditions. The three cases are ($Re = 60, \Delta\phi = 40^\circ$), ($Re = 150,$

$\Delta\phi = 100^\circ$), ($Re = 200, \Delta\phi = 90^\circ$). The first case at $Re = 60$ is in the longitudinal roll regime, the second two cases are in the boundary turbulence regime. We do not observe any significant variation of the latitudinal extent of the unstable region, $\Delta\theta$, with f^* in either the longitudinal roll or the boundary turbulence regimes. The dashed lines in Fig. 8 represent the mean values for each Re . Lower values of f^* in each data set would require lower Ekman numbers (i.e., faster turntable rotation rates) that are not accessible in our device.

Fig. 9a shows the latitudinal extent of the unstable region, $\Delta\theta$, as a function of the libration amplitude $\Delta\phi$ for fixed $f^* = 2/3$ and $Re = 60$ and two inner core sizes, $\chi = 0$ and 0.6 . In the range of parameters accessible with this device we observe a decay of the latitudinal extent in the longitudinal roll regime as we lower $\Delta\phi$. We note that a similar behavior was noted by Aldridge (1967) in a comparable range of parameters but with $f^* > 1$. The size of the inner core has only a marginal effect on the latitudinal extent of the instability.

In the boundary turbulence regime (Fig. 9b), we observe a saturation of the latitudinal extent for large libration amplitudes, respectively at $\Delta\theta = 50^\circ$ for $Re = 150$, $\Delta\theta = 65^\circ$ for $Re = 165$ and $\Delta\theta = 75^\circ$ for $Re = 175$ and 200 . For $\Delta\phi \lesssim 55^\circ$, we observe that the maximum latitudinal extent decreased with $\Delta\phi$. Experiments conducted at $Re = 165$ and 175 with two inner core sizes ($\chi = 0$ and 0.9) do not exhibit any measurable differences.

5. Discussion and planetary applications

In this study, we have found three different flow regimes induced inside a liquid cavity by the librational motion of the surrounding shell: (i) the stable boundary layer regime; (ii) the longitudinal roll regime; and (iii) the boundary turbulence regime. The onset of the longitudinal roll and boundary turbulence instability are governed by two critical boundary layer Reynolds numbers, respectively, $Re_{c1} \simeq 20$ and $Re_{c2} \simeq 120$.

5.1. Instability mechanism

Our results show that the librational driven instabilities are confined to the outer region of the fluid and do not penetrate the entire fluid volume. Furthermore, the flow patterns are qualitatively similar to Taylor and Taylor-Görtler instabilities, both of which are associated with a local centrifugal instability mechanism (e.g., Nakabayashi et al., 2002).

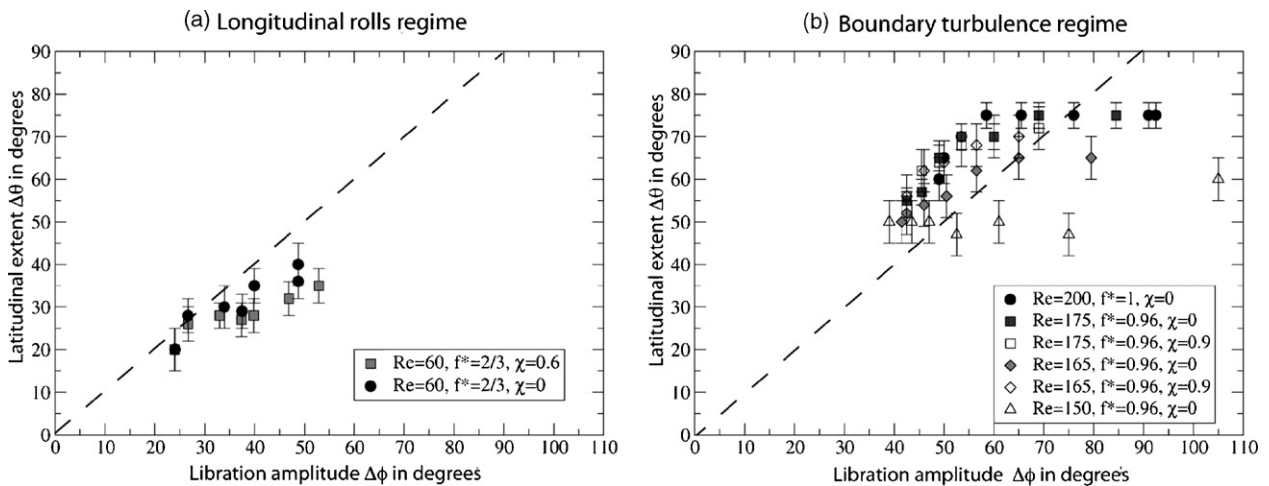


Fig. 9. (a) Latitudinal extent $\Delta\theta$ in the longitudinal roll regime as a function of the libration amplitude $\Delta\phi$ for fixed $Re = 60, f^* = 2/3$ and $\chi = 0$ and 0.6 . (b) Latitudinal extent $\Delta\theta$ in boundary turbulence regime as a function of the libration amplitude $\Delta\phi$ for $Re = 200 (f^* = 1, \chi = 0)$, $Re = 175 (f^* = 0.96, \chi = 0 \text{ and } 0.9)$, $Re = 165 (f^* = 0.96, \chi = 0 \text{ and } 0.9)$ and $Re = 150 (f^* = 0.96, \chi = 0)$. The dashed lines demarcate the maximum latitudinal extent for structures formed in the vicinity of the equator and advected poleward by the latitudinal Ekman circulation.

We propose that the longitudinal roll instability results from a centrifugal mechanism in the Ekman boundary layer, as first suggested by Aldridge (1967). Fig. 3a schematically shows the angular velocity of the overlying solid container. The fluid in the bulk of the cavity follows a nearly solid body rotation at the table's mean angular velocity Ω . In contrast, the fluid in the boundary layer is “spun-up” to faster rates during the prograde phase of the libration cycle. Similarly, the fluid in the boundary layer is then “spun-down” to slower rates during the retrograde phase of the libration cycle. Thus, a parcel of fluid displaced from the boundary layer to the bulk will experience a greater outward centrifugal force than the surrounding fluid during the prograde phase of the cycle. This will result in a stabilization of the system (Fig. 3b). In contrast, a parcel of fluid is displaced from the boundary layer to the bulk will experience a weaker centrifugal force than the surrounding fluid during the retrograde phase of the libration cycle. This will result in its further inward displacement. This “centrifugal instability” leads to the formation of the longitudinal rolls predominantly during the retrograde phase of each libration cycle (Fig. 3c).

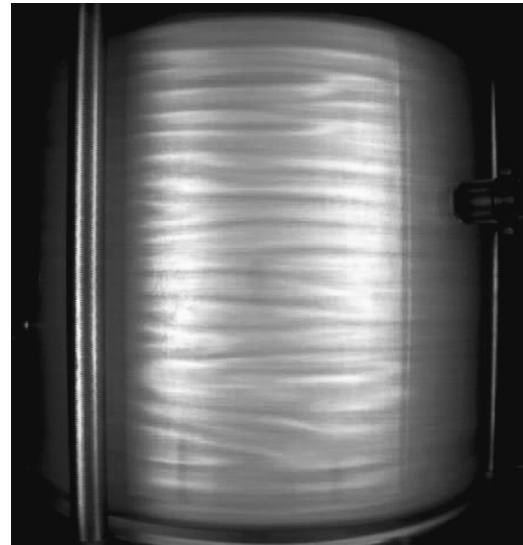


Fig. 10. Longitudinal rolls in a librating cylindrical tank ($H = 20$ cm, $R = 8.6$ cm), $\Delta\phi = 60^\circ$, $f^* = 0.5$, $E_H = 10^{-4}$, where E_H is the Ekman number based on the radius of the tank. This image shows the roll instability at the peak retrograde displacement of the tank ($\phi \simeq -60^\circ$), as measured in the rotating reference frame.

5.1.1. Latitudinal extent of the instability

A decrease of $\Delta\theta$ is observed with decreasing amplitude of libration both in the longitudinal roll and boundary turbulence regimes. In contrast, the frequency ratio f^* has a marginal effect on the extent of the unstable region. We discuss two possible models to account for the latitudinal extent of the unstable region. In the first model, the instabilities always develop in the vicinity of the equatorial plane and are advected by the poleward Ekman circulation during the retrograde phase of the libration cycle. In this model the latitudinal extent is bounded by the maximum latitude at which an equatorial structure can be advected poleward during the retrograde phase. In planetary settings the Ekman circulation is vanishingly small. Therefore, this model predicts that librational driven instabilities are confined to the equatorial region.

In the second model, the centrifugal destabilization arises at all latitudes where the local boundary layer Reynolds number is above its critical value. Although the poleward Ekman circulation during the retrograde phase may still play a role in this second model, it no longer provides an upper bound on the latitudinal extent of the unstable region. In contrast to the first model, this local instability model predicts a finite latitudinal extent of the unstable region at planetary settings. We now seek to determine which model best describes our results.

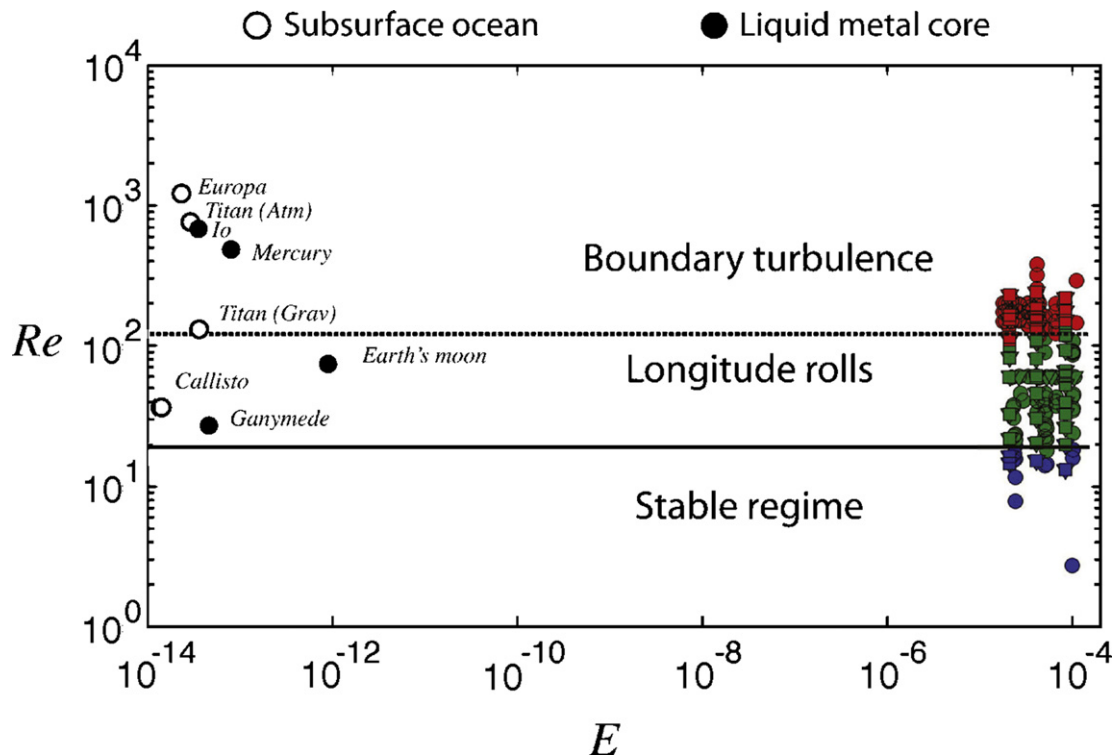


Fig. 11. Extrapolation of our results toward planetary conditions. Planetary Re and E -values are given in Table 2. Planets with a subsurface ocean are represented by open circles; planets with a outer liquid core are represented by filled circles. The symbols and colors for the experimental data at $E > 10^{-5}$ are the same as in Fig. 7.

At first order, we calculate the Ekman circulation and the θ -dependent Reynolds number based on a linear steady Ekman layer. Following (Greenspan, 1968) the Ekman boundary layer thickness is given by:

$$\delta(\theta) \propto E^{1/2} r_o \cos \theta \quad (13)$$

except at the equator and at the critical latitude in both hemispheres where it becomes singular (Roberts and Stewartson, 1963; Noir et al., 2001b). The horizontal components of the non-dimensionalized velocity in the Ekman boundary layer scales as (Greenspan, 1968):

$$u_\theta(\theta) \sim u_\phi(\theta) \propto \Delta \phi f^* \cos \theta \sin(f^* t). \quad (14)$$

Recent analytical work by Zhang and Liao (2008) have argued that the Ekman boundary layer thickness may not follow a $E^{1/2}$ scaling law for an oscillatory perturbation. However, a different scaling of the boundary layer thickness would still yield $u_\theta \sim u_\phi \propto \Delta \phi$ in the boundary layer in order to conserve mass.

From (14), we expect the latitudinal advection of flow structures in the Ekman boundary layer to be proportional to $\Delta \phi$. Further, the values of $\Delta \phi$ will provide an upper bound on the latitudinal advection as u_θ cannot be larger than u_ϕ , which is the source of the Ekman circulation. Integrated over a libration cycle, (14) shows that the net latitudinal advection should be independent of f^* , which is in agreement with our results (Fig. 8). Thus, $\Delta \theta = \Delta \phi$ will provide an upper bound on the latitudinal extent, $\Delta \theta$, in the first model. We refer to this limit as the advective upper bound.

We now define a θ -dependent Reynolds number, $Re(\theta)$, from (13) and (14), which now includes the latitude variations of the Ekman boundary layer thickness, $\delta(\theta) = E^{1/2} r_o \cos \theta$, and of the maximum local value of the shell's azimuthal velocity, $u_\phi(\theta) = \Delta \phi \omega_L \cos \theta$:

$$Re(\theta) = \Delta \phi f^* E^{-1/2} \cos^2 \theta. \quad (15)$$

If the onset of the instability is driven by a local destabilization of the boundary layer, the extent of the unstable region in the absence of advection can be defined by the maximum latitude θ_{\max} at which $Re(\theta_{\max}) = Re_c$.

The dashed lines in Fig. 9 denote the upper bound of $\Delta \theta$ for the latitudinal advection model. In the longitudinal rolls regime the latitudinal extent never exceeds the advective upper bound. In contrast, in the boundary turbulence regime, we observe instabilities at latitudes greater than the advective upper bound. This implies that the turbulent structures must have formed at finite latitudes above and below the equatorial plane before they were advected poleward. This supports a local destabilization mechanism, as in the second model, for $Re \gtrsim Re_{c2}$.

To further test the second model we have carried out a set of preliminary experiments in a right cylindrical tank of radius $R = 8.6$ cm and of height $H = 20$ cm. In this geometry the sidewall Reynolds number is independent of the vertical coordinate. Thus, if longitudinal rolls result from a local destabilization mechanism they should form simultaneously at all locations along the vertical sidewall. Fig. 10 shows longitudinal rolls in the cylinder experiment for $\Delta \phi = 60^\circ$, $f^* = 0.5$, $E_H = 10^{-4}$, where E_H is the Ekman number based on the radius of the tank. This image shows the roll instability at the peak retrograde displacement of the tank ($\phi \simeq -60^\circ$), as measured in the rotating reference frame. In agreement with a local destabilization mechanism, we observe that longitudinal rolls form simultaneously at all location along the vertical sidewall with no significant poleward advection.

From the results of Figs. 9 and 10, we argue that the librational driven instabilities develop from a local destabilization in the Ekman boundary layer at latitudes where $Re(\theta) > Re_c$. In our laboratory experiments, which are carried out using large libration amplitudes ($\Delta \phi \sim 30^\circ$ to 200°), the poleward advection by the Ekman circulation contributes to the latitudinal extent of the

unstable region. In contrast, in planetary settings, where libration amplitude and Ekman circulation are small, we expect that the latitudinal extent of the unstable region is controlled by the value of the local boundary layer Reynolds number, $Re(\theta)$.

5.2. Planetary applications

For librating planets that are believed to have internal fluid layers, the boundary layer Reynolds number can be estimated using (12). These Re estimates are given in Table 2. In Fig. 11 we extrapolate the critical values of Re found in our experiments to planetary parameter values. The estimates of Re for Mercury, Io, Titan and Europa are above $Re_{c2} \simeq 120$, whereas estimates for the Earth's moon, Ganymede and Callisto are between $Re_{c1} \simeq 20$ and $Re_{c2} \simeq 120$. Thus, our results suggest that boundary layer turbulence may exist in the molten cores of Mercury and Io and in the subsurface oceans of Titan and Europa. Using the proposed local destabilization model, we estimate the latitudinal extent of the turbulent region to be $\Delta \theta \sim 60^\circ$ for Mercury, $\Delta \theta \sim 65^\circ$ for Titan and Io, and $\Delta \theta \sim 70^\circ$ for Europa. For these planets, librational enhancement of viscous dissipation and of turbulent boundary stresses may be significant. In contrast, we predict that laminar longitudinal rolls exist in the molten cores of Earth's moon and Ganymede and in Callisto's subsurface ocean. Thus, librational enhanced viscous dissipation is less likely to produce a significant contribution to the energy budgets for these planets.

6. Conclusions and perspectives

In this paper we report that a spherical fluid cavity undergoing longitudinal forced libration is subject to both longitudinal roll and boundary turbulence instabilities. We show that the onset of the instabilities may be characterized by two critical boundary layer Reynolds numbers, respectively, $Re_{c1} \simeq 20$ and $Re_{c2} \simeq 120$. In addition, the instabilities are observed to be transient: they develop predominantly during the retrograde phase of the libration cycle and dissipate during the prograde phase. Both the longitudinal roll and turbulent instabilities develop in the vicinity of the outer boundary. We propose that these instabilities are primarily driven by a local centrifugal mechanism in the Ekman boundary layer. In further support of a local boundary layer mechanism, we find that the presence of a non-librating inner core of radius of up to $\chi = 0.9$ does not produce any measurable effect in our experiments.

Our results imply that librational driven boundary layer turbulence may exist up to high latitudes in the subsurface liquid regions of Mercury, Io, Titan and Europa; longitudinal rolls may exist in the liquid interior portions of the Earth's moon, Ganymede and Callisto. Thus, turbulent dissipation and coupling are likely to be relevant for Mercury, Io, Titan and Europa, but are less likely to be significant on the Earth's moon, Ganymede and Callisto.

Acknowledgements

This work was financially supported by NASA's PG&G program (award #NNG06G197G, #NNX07AK44G). Computational resources were provided by the San Diego Supercomputing Center (SDSC, award #EAR070012N). The authors would also like to thank Joel Neal, Rick Bayard, Afshin Yaghmaei, John Pokras and Ron Aurnou for engineering support; and Jose Sanchez, Ian Topham and Steve Grubweiser (UCLA SEAS Machine shop) for fabricating the experimental device.

References

- Aelbrecht, D., D'Hieres, G.C., Renouard, D., 1999. Experimental study of the Ekman layer instability in steady or oscillating flows. *Continental Shelf Research* 19 (15–16), 1851–1867.

- Al-Shamali, F.M., Heimpel, M.H., Aurnou, J.M., 2004. Varying the spherical shell geometry in rotating thermal convection. *Geophysical and Astrophysical Fluid Dynamics* 98 (2), 153–169.
- Aldridge, K.D., 1967. An experimental study of axisymmetric inertial oscillations of a rotating liquid sphere. Ph.D. Thesis. Massachusetts Institute of Technology.
- Aldridge, K.D., 1975. Inertial waves and earth's outer core. *Geophysical Journal of the Royal Astronomical Society* 42 (2), 337–345.
- Aldridge, K.D., Toomre, A., 1969. Axisymmetric inertial oscillations of a fluid in a rotating spherical container. *Journal of Fluid Mechanics* 37, 307.
- Andereck, C.D., Liu, S.S., Swinney, H.L., 1986. Flow regimes in a circular couette system with independently rotating cylinders. *Journal of Fluid Mechanics* 164, 155–183.
- Anderson, J.D., Jacobson, R.A., McElrath, T.P., Moore, W.B., Schubert, G., Thomas, P.C., 2001. Shape, mean radius, gravity field, and interior structure of callisto. *Icarus* 153 (1), 157–161.
- Anderson, J.D., Lau, E.L., Sjogren, W.L., Schubert, G., Moore, W.B., 1996. Gravitational constraints on the internal structure of ganymede. *Nature* 384 (6609), 541–543.
- Anderson, J.D., Schubert, G., Jacobson, R.A., Lau, E.L., Moore, W.B., Sjogren, W.L., 1998. Europa's differentiated internal structure: inferences from four galileo encounters. *Science* 281 (5385), 2019–2022.
- Aurnou, J., Heimpel, M., Wicht, J., 2007. The effects of vigorous mixing in a convective model of zonal flow on the ice giants. *Icarus* 190 (1), 110–126.
- Baca, S.M., Thomson, E.E., Kristan, W.B., 2005. Location and intensity discrimination in the leech local bend response quantified using optic flow and principal components analysis. *Journal of Neurophysiology* 93 (6), 3560–3572.
- Balogh, A., Giampieri, G., 2002. Mercury: the planet and its orbit. *Reports on Progress in Physics* 65 (4), 529–560.
- Blennerhassett, P.J., Bassom, A.P., 2007. The linear stability of high-frequency flow in a torsionally oscillating cylinder. *Journal of Fluid Mechanics* 576, 491–505.
- Breuer, D., Hauck, S.A., Buske, M., Pauer, M., Spohn, T., 2007. Interior evolution of mercury. *Space Science Reviews* 132 (2–4), 229–260.
- Christensen, U., Wicht, J., 2007. Numerical dynamo simulations. In: Schubert, G. (Ed.), *In: Treatise on Geophysics*, vol. 8. Elsevier.
- Coles, D., 1965. Transition in circular couette flow. *Journal of Fluid Mechanics* 21, 385.
- Comstock, R.L., Bills, B.G., 2003. A solar system survey of forced librations in longitude. *Journal of Geophysical Research-Planets* 108 (E9).
- Davis, S.H., 1976. The stability of time periodic flows. *Annual review of Fluid Mechanics* 8, 57–74.
- Faller, A.J., 1963. An experimental study of the instability of the laminar Ekman boundary layer. *Journal of Fluid Mechanics* 15 (4), 560.
- Faller, A.J., Kaylor, R.E., 1966. A numerical study of instability of laminar Ekman boundary layer. *Journal of the Atmospheric Sciences* 23 (5), 466.
- Glatzmaier, G.A., 1984. Numerical simulations of stellar convective dynamos. 1. The model and method. *Journal of Computational Physics* 55 (3), 461–484.
- Greenspan, H.P., 1968. *The Theory of Rotating Fluids*. Cambridge University Press, Cambridge.
- Hauck, S.A., Aurnou, J.M., Dombard, A.J., 2006. Sulfur's impact on core evolution and magnetic field generation on ganymede. *Journal of Geophysical Research-Planets* 111.
- Hauck, S.A., Dombard, A.J., Phillips, R.J., Solomon, S.C., 2004. Internal and tectonic evolution of mercury. *Earth and Planetary Science Letters* 222 (3–4), 713–728.
- Heimpel, M.H., Aurnou, J.M., Al-Shamali, F.M., Perez, N.G., 2005. A numerical study of dynamo action as a function of spherical shell geometry. *Earth and Planetary Science Letters* 236 (1–2), 542–557.
- Kerswell, R.R., Malkus, W.V.R., 1998. Tidal instability as the source for io's magnetic signature. *Geophysical Research Letters* 25 (5), 603–606.
- Kuskov, O., Kronrod, V., 2005. Internal structure of europa and callisto. *Icarus* 177, 550–569.
- Lilly, D.K., 1966. On instability of Ekman boundary flow. *Journal of the Atmospheric Sciences* 23 (5), 481.
- Lorenz, R.D., Stiles, B.W., Kirk, R.L., Allison, M.D., Del Marmo, P.P., Iess, L., Lunine, J.I., Ostro, S.J., Hensley, S., 2008. Titan's rotation reveals an internal ocean and changing zonal winds. *Science* 319 (5870), 1649–1651.
- Malkus, W., 1968. Precession of the earth as the cause of geomagnetism. *Science* 160, 777.
- Margot, J.L., Peale, S.J., Jurgens, R.F., Slade, M.A., Holin, I.V., 2007. Large longitude libration of mercury reveals a molten core. *Science* 316 (5825), 710–714.
- Murray, C.D., Dermott, S.F., 1999. *Solar System Dynamics*. Cambridge University Press, Cambridge.
- Nakabayashi, K., Zheng, Z., Tsuchida, Y., 2002. Characteristics of disturbances in the laminar-turbulent transition of spherical couette flow. 2. New disturbances observed for a medium gap. *Physics of Fluids* 14 (11), 3973–3982.
- Neitzel, G.P., Davis, S.H., 1981. Centrifugal instabilities during spin-down to rest in finite cylinders numerical experiments. *Journal of Fluid Mechanics* 102, 329–352.
- Noir, J., Brito, D., Aldridge, K., Cardin, P., 2001a. Experimental evidence of inertial waves in a precessing spheroidal cavity. *Geophysical Research Letters* 28 (19), 3785–3788.
- Noir, J., Jault, D., Cardin, P., 2001b. Numerical study of the motions within a slowly precessing sphere at low Ekman number. *Journal of Fluid Mechanics* 437, 283–299.
- Peale, S.J., Boss, A.P., 1977. Spin-orbit constraint on viscosity of a mercurian liquid core. *Journal of Geophysical Research* 82 (5), 743–749.
- Peale, S.J., Phillips, R.J., Solomon, S.C., Smith, D.E., Zuber, M.T., 2002. A procedure for determining the nature of mercury's core. *Meteoritics and Planetary Science* 37 (9), 1269–1283.
- Roberts, P.H., Stewartson, K., 1963. On stability of a maclaurin spheroid of small viscosity. *Astrophysical Journal* 137 (3), 777.
- Sohl, F., Spohn, T., Breuer, D., Nagel, K., 2002. Implications from galileo observations on the interior structure and chemistry of the galilean satellites. *Icarus* 157, 104–119.
- Spohn, T., Schubert, G., 2003. Oceans in the icy galilean satellites of jupiter? *Icarus* 161 (2), 456–467.
- Stewartson, K., Roberts, P.H., 1963. On the motion of a liquid in a spheroidal cavity of a precessing rigid body. *Journal of Fluid Mechanics* 17, 1–20.
- Tatro, P.R., Mollo-Christensen, 1967. Experiments on Ekman layer instability. *Journal of Fluid Mechanics* 28, 531.
- Tilgner, A., 1999. Driven inertial oscillations in spherical shells. *Physical Review E* 59 (2), 1789–1794.
- Tobie, G., Grasset, O., Lunine, J.I., Mocquet, A., Sotin, C., 2005. Titan's internal structure inferred from a coupled thermal-orbital model. *Icarus* 175, 496–502.
- Tokano, T., Neubauer, F.M., 2005. Wind-induced seasonal angular momentum exchange at titan's surface and its influence on titan's length-of-day. *Geophysical Research Letters* 32.
- Van Hoolst, T., Rambaux, N., Karatekin, Ö., 2008. The effect of gravitational and pressure torques on titan's length-of-day variations. *Icarus* (2008) doi:10.1016/j.icarus.2008.11.009.
- Van Hoolst, T.V., Rambaux, N., Karatekin, O., Dehant, V., Rivoldini, A., 2008. The librations, shape and icy shell of europa. *Icarus* 195 (1), 386–399.
- Vanyo, J., Wilde, P., Cardin, P., Olson, P., 1995. Experiments on precessings flows in the earth's liquid core. *Geophysical Journal International* 121, 136–142.
- Wahr, J.M., 1988. The earth's rotation. *Annual Review of Earth and Planetary Sciences* 16, 321–349.
- Weidman, P.D., 1976a. Spin-up and spin-down of a rotating fluid. 1. Extending wedemeyer model. *Journal of Fluid Mechanics* 77 (October 22), 685–708.
- Weidman, P.D., 1976b. Spin-up and spin-down of a rotating fluid. 2. Measurements and stability. *Journal of Fluid Mechanics* 77 (October 22), 709.
- Wicht, J., 2002. Inner-core conductivity in numerical dynamo simulations. *Physics of the Earth and Planetary Interiors* 132 (4), 281–302.
- Williams, J.G., Boggs, D.H., Yoder, C.F., Ratcliff, J.T., Dickey, J.O., 2001. Lunar rotational dissipation in solid body and molten core. *Journal of Geophysical Research-Planets* 106 (E11), 27933–27968.
- Williams, J.G., Dickey, J.O., 2002. Lunar geophysics, geodesy, and dynamics. In: *Proceedings of the 13th International Workshop on Laser Ranging*, Washington, DC.
- Williams, J.P., Aharonson, O., Nimmo, F., 2007. Powering mercury's dynamo. *Geophysical Research Letters* 34 (21).
- Wu, X., Bender, P.L., Peale, S.J., Rosborough, G.W., Vincent, M.A., 1997. Determination of mercury's 88 day libration and fluid core size from orbit. *Planetary and Space Science* 45 (1), 15–19.
- Yoder, C.F., 1995. Venus free obliquity. *Icarus* 117 (2), 250–286.
- Zhang, K., Liao, X., 2008. On the initial-value problem in a rotating circular cylinder. *Journal of Fluid Mechanics* 610, 425–443.